



HAL
open science

Understanding the Sn Loading Impact on the Performance of Mesoporous Carbon/Sn-Based Nanocomposites in Li-Ion Batteries

Cristina Nita, Julien Fullenwarth, Laure Monconduit, Jean-Marc Le Meins, Julien Parmentier, Moulay Tahar Sougrati, Camélia Matei ghimbeu

► **To cite this version:**

Cristina Nita, Julien Fullenwarth, Laure Monconduit, Jean-Marc Le Meins, Julien Parmentier, et al.. Understanding the Sn Loading Impact on the Performance of Mesoporous Carbon/Sn-Based Nanocomposites in Li-Ion Batteries. *ChemElectroChem*, 2018, 5 (21), pp.3249-3257. 10.1002/celec.201800835 . hal-02464997

HAL Id: hal-02464997

<https://hal.science/hal-02464997>

Submitted on 6 Feb 2020

HAL is a multi-disciplinary open access archive for the deposit and dissemination of scientific research documents, whether they are published or not. The documents may come from teaching and research institutions in France or abroad, or from public or private research centers.

L'archive ouverte pluridisciplinaire **HAL**, est destinée au dépôt et à la diffusion de documents scientifiques de niveau recherche, publiés ou non, émanant des établissements d'enseignement et de recherche français ou étrangers, des laboratoires publics ou privés.

Understanding the Sn loading impact on the performances of mesoporous carbon/Sn based nanocomposites in Li-ion batteries

Cristina Nita ^{[a],[b]}, Julien Fullenwarth ^{[c],[d]}, Laure Monconduit ^{[c],[d]}, Jean-Marc Le Meins ^[a], Julien Parmentier ^[a], Moulay Tahar Sougrati ^{[c],[d]}, Camélia Matei Ghimbeu ^{[a],[d]}*

Abstract: Herein, we report a systematic study on the understanding of the influence of tin metal precursor salt amount on the formation of carbon/tin hybrid materials and their performances as anode in Li-ion batteries. Small Sn metallic particles (≈ 5 nm) covered by a SnO₂ layer were uniformly dispersed in a mesoporous carbon for low loading of tin, while for higher Sn loading the formation of Sn-based particles aggregates (~ 200 nm) is promoted as well. By increasing the Sn loading from 20 to 80%, the irreversible capacity was successfully reduced and the reversible capacity improved. This could be mainly related to the decrease of the C/Sn hybrids specific surface area and the increase of the Sn active species. For long term cycling, capacity fading was observed particularly for high Sn loadings and assigned to the Sn nanoparticles placed outside the carbon network which upon lithiation witness large volume expansion leading to severe particle growth and agglomeration. Therefore, similar reversible capacities at long cycling are reached no matter the Sn loading. For optimal electrochemical performances, it appears that a balance between the amount of Sn and uniform small Sn-based particles dispersion within carbon matrix must be assured in order to design high performance anode for Li-ion batteries.

Introduction

During the last years, the interest for environmentally friendly processes and alternative sources dedicated to energy generation and storage has significantly increased. For electrical vehicles and portable electronics applications, the Li-ion batteries have been considered the most important power

sources due to their high energy density, operating voltages and lightweight design ^[1]. However, the fast development of the technology demands high performing batteries, but in the same time safety and low-cost.

A Li-ion battery contains several components, each of these contributing in different ways to the improvement of the battery performances, the anode inducing a significant impact ^[2]. Nowadays, graphite is the most used anode in Li-ion batteries, with a theoretical capacity limited to 372 mAh g⁻¹, because of the limited Li storage capacity (one Li atom for six carbon atoms) ^[3]. In order to improve the capacity as compared to graphite an increasing interest was focused on other anode materials. For such purposes, the Sn or Sn-based materials have been considered among the best candidates, especially due their higher theoretical capacity (781 mAh g⁻¹ for SnO₂ ^[4] and 990 mAh g⁻¹ for Sn ^[5]). However, such metals suffer an important volume expansion during lithiation step and therefore, particles agglomeration and electrode pulverization occurs along with the loss of electrochemical performances. These drawbacks could be overcome by downsizing the Sn particle size ^[6] and by using different carbon materials (carbon nanotubes ^{[7],[8]}, carbon fibers ^[9], carbon nanospheres ^[10], graphenes ^[11], graphite ^[12], mesoporous carbon ^{[3],[13]}) as supports for Sn-based hybrid materials. This allow to alleviate the macroscopic volume expansion of the composite material and, in the same time, increase its electrical conductivity and provide efficient pathways for electrolyte diffusion as demonstrated by several works ^{[14],[15],[16],[17]}.

Wu *et al.* ^[18] reported the preparation of SnO₂-CNTs using glucose through a hydrothermal approach, followed by a carbonization at 500°C in nitrogen atmosphere. The materials present a discharge capacity of 400 mAh g⁻¹ at current density of 100 mA g⁻¹, after 50 cycles, slightly higher than that of graphite, but lower than the theoretical capacity of the composite because of the solid-electrolyte interphase (SEI) formation. Cui *et al.* ^[17] reported the preparation of Sn/onion-like carbon nanocapsules by arc discharge method with a reversible capacity of 585 mAh g⁻¹ after 100 cycles at very low current rate, 100 mA g⁻¹, while Han *et al.* ^[16] succeeded to increase the capacity up to 902 mAh g⁻¹ (at 100 mA g⁻¹ after 1000 cycles) by introducing nitrogen (N) atoms in the carbon framework. The high capacity and the stable cycling could be promoted by the very low current rate used. Another limitation is the complexity of the synthesis procedure which involves specific pressure and temperature conditions. Guo *et al.* ^[10] prepared Sn nanoparticles embedded in N-doped hollow nanosphere which delivered 500 mAh g⁻¹ at 5C after 500 cycles. Nano size tin particles embedded in porous multichannel carbon microtubes were synthesized by electrospinning and provided a capacity of 350 mAh g⁻¹, at 2 C rate after 600 cycles ^[19]. Liu *et al.* ^[20] reported capacities up to 520 mAh g⁻¹ at 500 mA g⁻¹, after 1000 cycles, for Sn/N-doped carbon nanospheres prepared by arc discharge method. Jahel *et al.* ^{[21],[3]} pointed out that the confinement of electrochemically active SnO₂ nanoparticles (ca. 2 nm in diameter) in the pores of a mesoporous carbon is the key parameter to avoid the particle growth and agglomeration, affording high capacity and long

[a] Dr. C Nita, Dr. J-M Le Meins, Dr. J Parmentier, Dr. C. Matei Ghimbeu

Université de Strasbourg, Université de Haute-Alsace, Institut de Science des Matériaux de Mulhouse, UMR 7361, CNRS
Address : 15 rue Jean Starcky, BP 2488, 68057 Mulhouse Cedex, France

E-mail: camelia.ghimbeu@uha.fr

[b] Dr. C Nita

Center for Advanced Laser Technologies (CETAL), National Institute for Lasers, Plasma and Radiation Physics, Atomistilor 409 bis, RO-77125, Magurele, Romania

[c] J. Fullenwarth, Dr. L. Monconduit, Dr. M T Sougrati
CG/AIME (UMR 5253 CNRS), Université Montpellier II CC 15-02
Place E. Bataillon, 34095 Montpellier Cedex, France

[d] J. Fullenwarth, Dr. L. Monconduit, Dr. M T Sougrati, Dr. C Matei Ghimbeu
Réseau sur le Stockage Electrochimique de l'Energie (RS2E) CNRS FR3459
33 Rue Saint Leu, 80039 Amiens Cedex, France

Supporting information for this article is given via a link at the end of the document.

stable cycling life (up to 2000 cycles). The improvement of the C/SnO₂ anode materials performances was achieved, with a reversible charge capacity up to 443 mAh g⁻¹ at 1C current rate after 2000 cycles. However, the irreversible capacity of the first charge-discharge cycle was still high, the later one remaining still an important problem of such materials and is mainly related to several factors as enumerate next: (i) solid electrolyte formation due to the reactions of the electrolyte with the high surface area of the porous carbon support, ii) the electrolyte consumption due to the reduction of tin oxide species to Sn metallic phase, according to the reaction described in [3] and iii) the small amount of active phase (40 wt.% SnO₂, corresponding to 31 wt.% Sn) in the composite, and therefore, the high amount of carbon (with a low electrochemical activity after the first discharge).

In order to overcome these drawbacks, the present study aims to systematically investigate the influence of Sn-based nanoparticles loading on the irreversible capacity, the reversible capacity and the cycle stability of carbon/Sn hybrids. As far as we know and highlighted by the literature review gathered in Table 1, no systematic study have been performed until now for Sn/C hybrids to evaluate how the Sn/SnO₂ loadings can influence the formation of Sn/C hybrid materials (particle size, surface chemistry and porosity) and further impact their electrochemical performances in Li-ion batteries. In addition, the contribution of each component (carbon and Sn) to the irreversible/reversible capacity and the long term cycling is not addressed either to our knowledge. The improvement of irreversible and reversible capacity in the first cycles compared to the commercial graphite anode by adding high amounts of Sn, as well as the capacity fading behavior with further cycling is discussed in the light of material characteristics (nanoparticle dispersion/confinement in the carbon mesopores, amount of SnO₂ present in the nanoparticles and specific surface area).

Table 1. Carbon/Sn-based materials for lithium-ion battery.

Carbonaceous /Sn-based material	Preparation method of composite	Electrochemical performances vs. Li			Refs
		Current density (mA g ⁻¹)	Reversible capacity (mAh g ⁻¹)	Cycles number	
Onion-like carbon NCs/Sn NPs	Arc-discharge method	100	585	100	[17]
Sn nanocapsules/N-doped onion-like carbon	Arc-discharge method	100	902	1000	[16]
Sn nanowires/Carbon nanotubes	Chemical vapor deposition (CVD)	100	420-630	30	[8]
Sn/Carbon core-shell	Hydrothermal method, Heat treatment	100	400	50	[22]
Sn nanoparticles/N-doped hollow nanosphere	Solvothermal method	0.2 C	1070	200	[10]
		5 C	500	500	

Sn/carbon nanotubes composite	Acid-etching treatment	30	413	100	[15]
Sn NPs/Carbon nanotubes nanocapsules	Direct current (DC) arc-discharge method	100	600	10	[14]
SnO ₂ nanocrystals/carbon nanotubes	Solvothermal method	200	497	300	[23]
SnO ₂ /carbon nanotubes	Solvothermal method	100	709	100	[7]
SnO ₂ /Carbon nanotubes	Hydrothermal approach	100	400	50	[18]
Sn/N-doped carbon nanospheres	Arc-discharge method	500	520	1000	[20]
Sn NPs/carbon microtubes	Electrospinning, carbonization	2C	350	600	[19]
Sn particles/Carbon fibers	Impregnation/heat treatment	0.1 C	740	160	[9]
Sn/graphite	Electrocatalysis	C/15	433	35	[12]
Sn NPs /carbon/ graphene	Hydrothermal process	100	662	100	[11]
Sn/carbon nanocomposite	Sol-gel carbothermal reduction	20	588	200	[5]
Sn/porous carbon		100	788	300	[24]
Sn/mesoporous carbon	Sol-gel polymerization	20	400	15	[13]
SnO ₂ /Mesoporous carbon	Impregnation Heat Treatments	1 C	511	500	[3]
		200	367	2000	

Results and Discussion

Material characterization

Mesoporous carbon materials with embedded Sn nanoparticles were synthesized and characterized in order to study the influence of Sn loading on the C/Sn hybrid material characteristics and performances. The idea of using carbons with tunable pore size was motivated by our previous work [3], [21] where we have shown that the confinement of small SnO₂ nanoparticles inside the pores is the key parameter to avoid NPs agglomeration and to ensure long and stable cycle life in the battery.

The XRD pattern of mesoporous carbon exhibits three diffraction peaks, corresponding to the hexagonal graphite structure (Figure S1a, Supporting Information). The presence of broad peaks indicates a low degree of graphitization. SAXS patterns (Figure S1b, Supporting Information) display an intense peak at 0.97° (2 theta) sign of the presence of a mesoporous structure which is confirmed by TEM images revealing a worm-like structure with mesopores having relatively uniform size (Figure S1c, Supporting Information).

For C/Sn hybrid materials, the XRD patterns exhibit several intense peaks which were all indexed to the tetragonal Sn phase (pdf 00-004-0673) (Figure 1). A small quantity of SnO_2 is also formed as evidenced by the small and large (211) peak at 51° (2theta), noted \blacklozenge [19]. This oxide is probably present as a layer formed around the Sn nanoparticles and it could be formed during the "exposure" of the sample in air, since it is well known that smaller the nanoparticles are, easier their oxidization is [25] but also can be due to incomplete reduction of the Sn-based precursor. The nature and amount of such oxide layer is worth to be investigated in more detail since it is electrochemically active in the battery and contributes to the active mass of the samples.

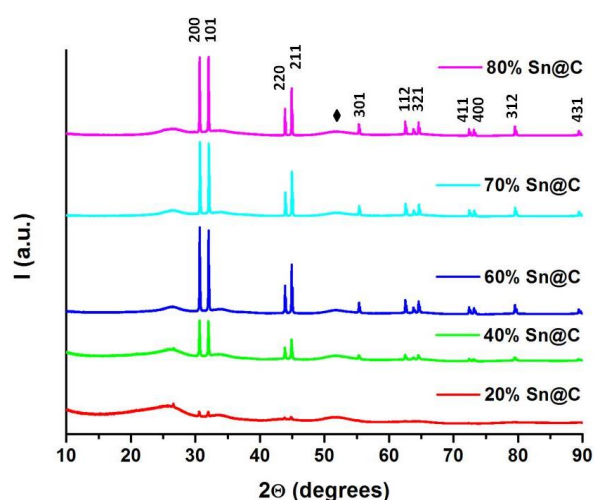


Figure 1. XRD patterns for C/Sn hybrid materials with different Sn loading (x% Sn@C, x=20/40/60/70/80).

If the structure of the materials was not changed by varying Sn loading, the size of the Sn crystallites seems to be significantly influenced. Particle size information was extracted by two complementary experiments: TEM and powder XRD. For this last one, the crystallite sizes which are related to size of domains over which diffraction is coherent (later called "apparent size") were extracted from the FWHM (full width at half maximum) of individual diffraction line profile via WinPlotr [26], DIFFRAC.EVA [27] and then using the Scherrer formula [28]. Main objective is to obtain a trend for the same family of compounds. Instrumental resolution function of the diffractometer was taken into account for the calculation because of the rather low FWHM values but let us keep in mind the limitation of the method according to the different hypothesis it involves (Gaussian peak profiles, size distribution not too large, etc...). The selected Sn reflection for this study is (200) which is the most intense, not too affected by asymmetric profile and with no peak overlap. Anisotropic line broadening is not observed for all these hybrid materials. This study allows to see the variation of the apparent size of the Sn crystallites as a function of the Sn loading (Table 2). For materials with different Sn loading, the apparent crystallite size increases with the Sn content from 67 nm for 20 wt.% of Sn to 148 nm for 80 wt.% of Sn. This tendency is in agreement with Oswald ripening mechanisms and in line with our previous work [29], [30].

Insights in the structure and morphology of the different materials were assessed by STEM (Figure 2). All the composites display small particles, uniformly distributed in the carbon matrix, but also bigger particles are present as aggregates. The HRTEM images allow to estimate a size of primary particles of about ~5nm (Figure S2e, Supporting Information). The homogeneous distribution of the smallest particles suggest that the wet impregnation/reduction protocols allow a good diffusion of Sn^{4+} and BH_4^- species in the porous carbon framework. Few aggregates with diameters ranging between 50 to 200 nm can be distinguished, especially for materials with high Sn loading (70%Sn@C and 80%Sn@C). For the larger particles, their size increases with the loading as shown previously [29], [30] and also observed by XRD microstructural analysis (Table 2). The large size of the agglomerated particles justifies also the high and very sharp XRD peaks (Figure 1).

In addition to TEM, the energy dispersive X-ray (EDX) mapping of the C/Sn-based materials confirms the uniform dispersion of Sn in the carbon support as well as the presence of aggregates (Figure S2, Supporting Information).

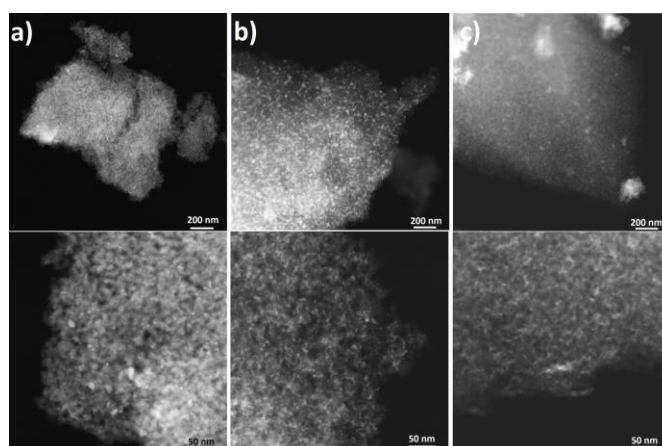


Figure 2. STEM images for carbon/Sn-based hybrid materials having different loadings corresponding to 20 wt.% Sn (a), 60 wt.% Sn (b); 80 wt.% Sn (c).

The most encountered problem, and rarely evaluated in the literature was related to the quantification of the Sn particles loading in the carbon framework and usually this problem is not addressed in many works. By considering the XRD results, it was demonstrated that the materials contains carbon, metallic Sn and SnO_2 . The composition and thermal/chemical stability of C/Sn-based hybrid materials were determined by TGA in air (Figure S3a, Supporting Information), which allows the combustion of carbon and determination of final SnO_2 quantity, coming both from the initial SnO_2 content, but also from the oxidation of metallic Sn during TGA under air (Table 2). The amounts of SnO_2 obtained varies between 14 and 89 wt.%. However, only the TGA results do not allow to discriminate between the initial Sn and SnO_2 in the hybrid materials. Therefore, complementary experiments to determine Sn/ SnO_2 ratios of the materials were performed by Mössbauer spectroscopy (Figure 3, Table 2).

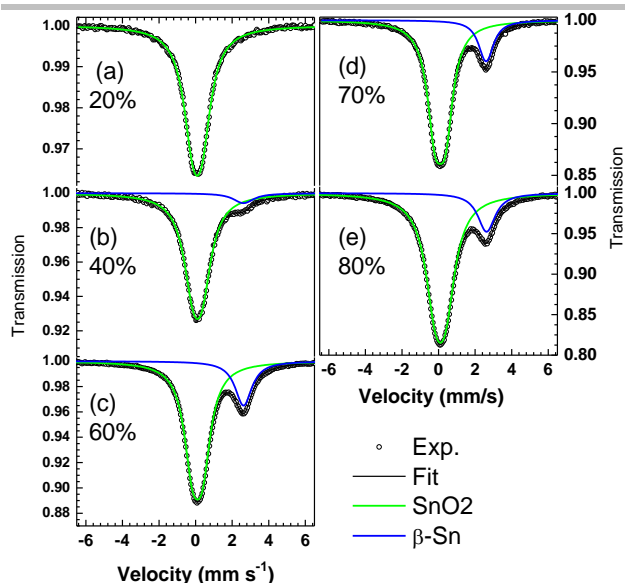


Figure 3. Room temperature Mössbauer spectra for carbon/Sn-based materials having different Sn loadings $x\%Sn@C$ ($x=20/40/60/70/80$).

Spectra obtained with different Sn loadings and carbon supports were fitted with 2 unresolved doublets corresponding to SnO_2 (green) and metallic tin (blue). SnO_2 has an isomer shift of 0.0-0.01 mm/s and a quadrupole splitting of 0.51-0.57 mm/s, while tetragonal Sn (β -Sn) has an isomer shift of 2.51-2.53 mm s^{-1} and a quadrupole splitting of 0.14-0.26 mm s^{-1} . The results confirm the presence of both compounds: Sn and SnO_2 . The Sn/ SnO_2 ratio measured by Mössbauer spectroscopy increases in the increase of Sn loading in the composite (ratio from 31.6/68.4 to 60.5/39.5 Sn/ SnO_2 for Sn loading ranging from 40% to 60% wt, Table 2). For high loadings (samples with 70 and 80 wt.% Sn), increase of the Sn loading does not induce a significant evolution of the Sn/ SnO_2 ratios.

The amount of formed SnO_2 may be explained by two factors, i.e, the particle size and particle location in the carbon network. On one hand, the Sn crystallites size increases from 67 nm to 148 nm (Table 2) when increasing the loading from 20 to 80% and the oxidation tendency generally increases with the decrease of the particle/crystallite size [25], [31]. However, starting with 60% of loading, a slight increase of SnO_2 amount is observed (Table 2) and this may be probably related to the higher amount of agglomerated Sn particles situated on the carbon surface, therefore, not confined in carbon pores (Figure 2) and more exposed to oxidation.

For 20%Sn@C sample, the metallic Sn quantity is so low (limit of detection) that it can hardly be detected by Mössbauer, especially because of the Lamb-Mössbauer factor which is ten times smaller for Sn than for SnO_2 [32]. So, for the future calculations and experiments it will be assumed that the 20%Sn@C sample contains only SnO_2 .

Based on Mössbauer results which provided the Sn to SnO_2 ratio in each composite, the amounts of Sn and SnO_2 could be determined taking into consideration the TGA results and further used to correctly assess the electrochemical performances (Table 2).

Table 2. Crystallite size determined by XRD and quantification of Sn and SnO_2 amounts contained in the Sn/C materials, based on Mössbauer spectroscopy and TGA analysis.

Material	Crystal lites Size (nm)	Sn and SnO_2 relative quantities by Mössbauer (%)		SnO ₂ by TGA (wt.%)	Initial quantities by TGA and Mössbauer (wt. %)	
		SnO ₂ (Sn (IV))	Sn (β - Sn)	SnO ₂	Sn	
20%Sn@C	67	100	0	14	14	0
40%Sn@C	78	68.4	31.6	21	14.4	6.6
60%Sn@C	107	39.6	60.4	56	22.1	33.7
70%Sn@C	110	44.8	55.2	66	29.7	36.6
80%Sn@C	148	46.9	53.1	89	41.7	47.3

The composition and chemical oxidation state of Sn on the surface of the materials (<10 nm thickness) were determined by XPS measurements (Figure S3b, Supporting Information and Table 3). Thus, the C1s, O1s and Sn3d peaks were detected. For all materials, two peaks are observed on the Sn 3d spectra and the separation binding energy between them is always 8.4 eV, which is in good agreement with the energy splitting of Sn and SnO_2 [21]. The shift of the peak positions for 20%Sn@C material could be induced by the high amount of SnO_2 , confirmed also by Mössbauer spectroscopy (Table 2), which is less conductive than the metallic Sn. The Sn amount increases by increasing the loading from 26.7 wt.% for 20%Sn@C to 72.1 wt.% for 80%Sn@C, while the atomic ratio O/Sn is comprised between 1.66 and 1.9 which confirms the presence of a SnO_2 layer in the surface of the material (Table 3).

The textural properties of the carbon and composite materials (specific surface area, porous volume and pore size) were evaluated by N_2 physisorption technique (77K). A mixture of type I/IV isotherms characteristic to micro/mesoporous materials [3] were observed in all cases (Figure 4a). The low relative pressure up-takes evidence the presence of micropores (size < 2 nm). The microporous volume (V_{micro}) of the carbon support is about 0.28 $cm^3 g^{-1}$, with a high BET specific surface area (SSA) of 665 $m^2 g^{-1}$ (Table 4).

Table 3. The chemical composition of the carbon/Sn-based materials obtained by XPS analysis.

Material	Composition, wt %			Repartition of oxygen, wt%		
	C	Sn	O	O-(C)	O-(Sn)	O-(Sn)/Sn
20%Sn@C	61.8	26.7	11.5	4.7	6.8	1.90
40%Sn@C	45.3	41.2	13.5	3.1	10.4	1.88
60%Sn@C	11.8	69.9	18.2	2.6	15.6	1.66
80%Sn@C	8.8	72.1	19.2	2.7	16.5	1.69

The total porous volume (V_T) for carbon is 0.97 $cm^3 g^{-1}$, indicating a mesoporosity size of 0.69 $cm^3 g^{-1}$ which could allow the accommodation of the Sn-based nanoparticles. The Sn addition induces a decrease of the N_2 adsorbed volume proportional with the Sn loading (Figure 4a). The evolution of the porous volume and SSA with the Sn loading are presented in the Figure 4c, d and Table 4. The V_{micro} decreases from 0.21 $cm^3 g^{-1}$ for 20%Sn@C to 0.07 $cm^3 g^{-1}$ for 80%Sn@C, while the SSA go down to 181 $m^2 g^{-1}$. The V_T presents the same decreasing trend from 0.79 $cm^3 g^{-1}$ for 20%Sn@C to 0.17 $cm^3 g^{-1}$ for 80%Sn@C, inducing the same behavior for the V_{meso} values.

As can be noticed (Fig. 4c), the mesoporous volume decrease more than microporous volume when increasing the Sn loading, suggesting a more preferential location of the particles in larger pore. This is rather related to the size of the Sn particle ~5 nm which can be better accommodated in mesopores having sizes of about 8 nm as will be discuss latter than in micropore having size < 1nm.

The pore size distribution (PSD) was obtained from the adsorption branch of the N₂ isotherms using 2D NLDFT model. The results show the presence of two types of pores: micropores (~ 0.8 nm) and mesopores (~ 8 nm) (Figure 4b). In contrast with the SSA and porous volumes, the pore size distribution before and after Sn/SnO₂ impregnation remains constant no matter the Sn loading. The presence of both types of pore are important, since they allow the diffusion of the electrolyte through the material and particularly the larger pores may accommodate the Sn particles and avoid their expansion/agglomeration during cycling.

Therefore, the incorporation of the Sn/SnO₂ nanoparticles induces a decrease in the surface area and porous volume. This may be explained mainly by two factors: i) higher density of metallic Sn-based particles than carbon, ii) confinement of the particles in the carbon pores (pore blockage with the particles). To discriminate between these two effects, the textural values were calculated per gram of carbon based on Sn and SnO₂ contents determined in Table 2. For low loadings ranging from 20 to 40%, the SSA and porous volume calculated per gram of carbon are similar to that of pristine carbon (C), while for high loadings i.e., 60 to 80 %, surprisingly these values gradually increases (Figure 4d). Two hypotheses may be proposed for this behavior: modification of carbon during the Sn⁴⁺ infiltration/reduction/drying steps or the existence of some porosity induced by Sn aggregates.

To check the first hypothesis, the composite was washed with HCl to remove the Sn/SnO₂ particles followed by several analytical characterizations to confirm the efficiency of such treatment (Figure S4, Supporting Information). XRD pattern of the material after washing (60%Sn/C@HCl) reveals the absence of Sn peaks and the presence of specific phase of carbon with low degree of graphitization.

Table 4. Textural values of carbon support and x% Sn@C materials (x=20/40/60/70/80).

Material	BET SSA m ² g ⁻¹	V _T cm ³ g ⁻¹	V _{micro} cm ³ g ⁻¹	V _{meso} cm ³ g ⁻¹
C	665	0.97	0.28	0.69
20%Sn@C	485	0.79	0.21	0.58
40%Sn@C	404	0.66	0.17	0.49
60%Sn@C	322	0.45	0.13	0.32
70%Sn@C	249	0.28	0.12	0.16
80%Sn@C	181	0.17	0.07	0.11

In addition, the TGA analysis in air indicates as well the complete removal of Sn-based nanoparticles since no SnO₂ residue was observed after thermal treatment, the curve of 60%Sn/C@HCl is overlapped to that of carbon one. The N₂ adsorption/desorption isotherms, present similar profiles to the pristine carbon support, suggesting that the carbon texture was not either modified by the synthesis procedure. Therefore, all these characterization point out that the carbon matrix texture, structure and thermal stability is not affected by the Sn nanoparticles synthesis procedure. However, for other metallic systems confined in microporous carbon, the modification of

carbon porosity (specific surface area and pore size) could be observed due to the synthesis procedure [29].

The second hypothesis assumes some porosity coming from the small size of Sn particles or between the Sn-particles. The Sn/SnO₂ can be considered non-porous, with no intrinsic porosity. However, due to their nanometric size, the SSA may increase and an inter-particle porosity cannot be excluded as well. This porosity increases due to the fact that, by increasing the particle loading, more Sn particles are formed outside the carbon network and they may contribute to the SSA increase. In the same time, a part of particles can be confined in the pores of carbon leading to lower SSA and pore volume.

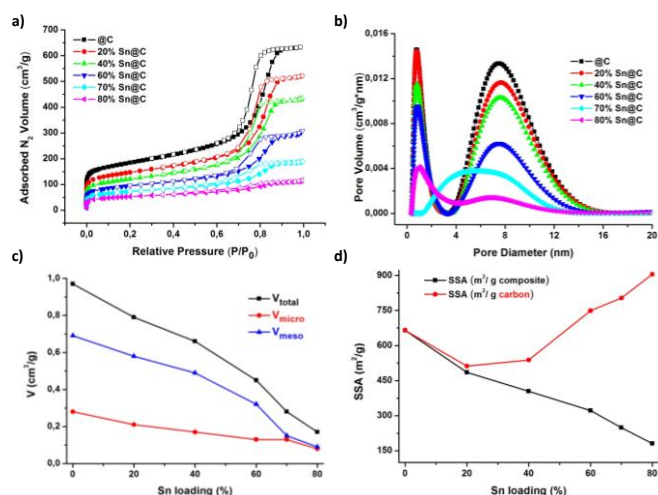


Figure 4. Textural properties for carbon and carbon/hybrid materials. N₂ adsorption/desorption isotherms (77K) (a) and pore size distribution (b). The evolution of the porous volume (c) and SSA (d) with the Sn loading.

Electrochemical performances

From the physico-chemical analyses on the C/Sn-based materials, we observed that the modification of the Sn loading produces changes regarding the size and dispersion of the Sn-based particles, their tendency to form agglomerates by increasing the Sn loading being highlighted. The Sn nanoparticles were found to be partially oxidized, and such oxide may play a role on the irreversible capacity. The textural properties such as SSA and porous volumes decreased with increasing of the Sn loading. All these characteristics may influence on the Li-ion batteries performances will be discussed in the following part.

The electrochemical tests for carbon and carbon/Sn-based materials were performed at constant (C/5) and variable current rate (between C/10 and 3C) in the voltage range of 0.01-1.5 V (vs Li/Li⁺). Figure 5 presents the galvanostatic and derivative curves for 60%Sn@C for the specified cycles. The first discharge profile show a rapid voltage drop to 1.5 V, followed by a gradually decrease down to 0.01 V, delivering a discharge capacity of 1480 mAh g⁻¹. The subsequent discharge curves are very different compared to the first one because of the formation of SEI on the surface of the anode during the first discharge. In the same time, the following curves are almost overlapped, indicating the good reversibility of the chemical reactions in the electrode and a good cycling stability. The initial charge capacity is 646 mAh g⁻¹, corresponding to a coulombic efficiency of 89%.

The derivative curves (Figure 5b) for the first discharge present three peaks badly defined at 0.63, 0.050 and 0.38 V, the first one being shifted to 0.42 starting for the second cycle. During charge three better defined derivative peaks are at 0.60, 0.72 and 0.80 V, in good agreement with those assigned to the reversible lithiation of Sn into Li Li₂Sn₅, LiSn and Li_{2.5}Sn, respectively (Eq. 2) [2].

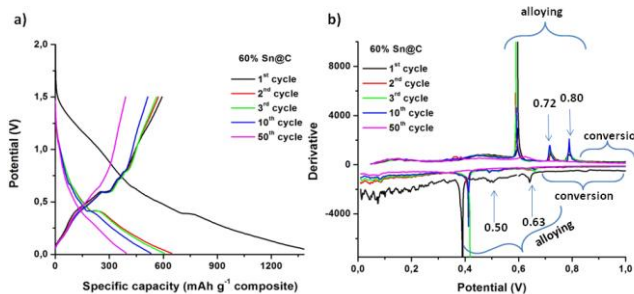
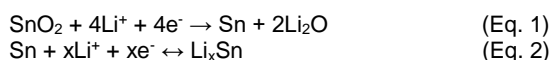


Figure 5. Galvanostatic (a) and derivative curves (b) for carbon/Sn composites 60%Sn@C at C/5 current rate in the voltage range of 0.01–1.5 V (vs. Li/Li).

Note that no clear peak appears around 1 V in discharge which would have been ascribed to the conversion reaction (Eq. 1) [33],[2] and this may be due to the nanometric size of Sn particles. After 50 cycles the peaks are no more visible.



To evidence the contribution of the carbon support on the electrochemical results of C/Sn hybrid materials, the carbon support, was tested in the same conditions as the composite materials (Figure 6). The reversible capacity of carbon support after 100 cycles was 204 mAh g⁻¹, but a high irreversible capacity of 776 mAh g⁻¹ was observed during the first charge-discharge cycle, representing 78% from the first charge capacity (Table S1a, Supporting Informations). The coulombic efficiency is quite low in the first cycle ($\approx 16\%$), but from the second one, it strongly increases to 80% and after 25 cycling reaching 100% (Figure 6a). The high irreversible capacity and the low coulombic efficiency in the first cycles are related to the high surface area of carbon materials which induces the electrolyte decomposition with the formation of a solid electrolyte interphase.

The electrochemical performances of the hybrid materials were evaluated at constant and variable current rate and compared with their theoretical capacities (Figure 6). The theoretical capacity for each material was calculated by taking into account the real amount of each compound (Sn/SnO₂/C) (Table 2), with the theoretical capacities for Sn and SnO₂ (990 mAh g⁻¹ [5] and 781 mAh g⁻¹ [4], respectively) and the experimental reversible capacity obtained for the carbon which was used as support.

The irreversible capacity of C@Sn composite materials is even higher than the carbon one, suggesting a contribution of Sn-based nanoparticles to the irreversible capacity (Figure 6b). In order to determine the impact of Sn-particles on the irreversible capacity, we calculated its contribution by taking into account the experimental irreversible capacities obtained for the carbons support.

As can be noticed a decrease of the irreversible capacity with the decrease of the carbon content in the C@Sn composites is clearly observed. The 20%Sn@C presents an irreversible capacity of 1323 mAh g⁻¹, from which 667 mAh g⁻¹ due to the carbon while by increasing the Sn loading to 80%, the irreversible capacity was reduced to 653 mAh g⁻¹ (43%). These values are lower than those of Sn powder, where an irreversible capacity around 1350 mAh g⁻¹ representing 93% from the initial capacity was reported in the literature [34]. The significant decrease of the irreversible capacity for 80%Sn/C compare to that of Sn powder (93%) and, in the same time, to the irreversible capacity of the carbon support (78%) indicates the importance of carbon matrix.

This decrease tendency of irreversible capacity may be related to the decrease of the specific surface area of the C@Sn materials, as demonstrated by the rather linear correlation of

irreversible capacity with the specific surface area (Figure 6c). The presence of a smaller fraction of porous carbon limits the electrolyte decomposition and the solid electrolyte interphase (SEI) formation.

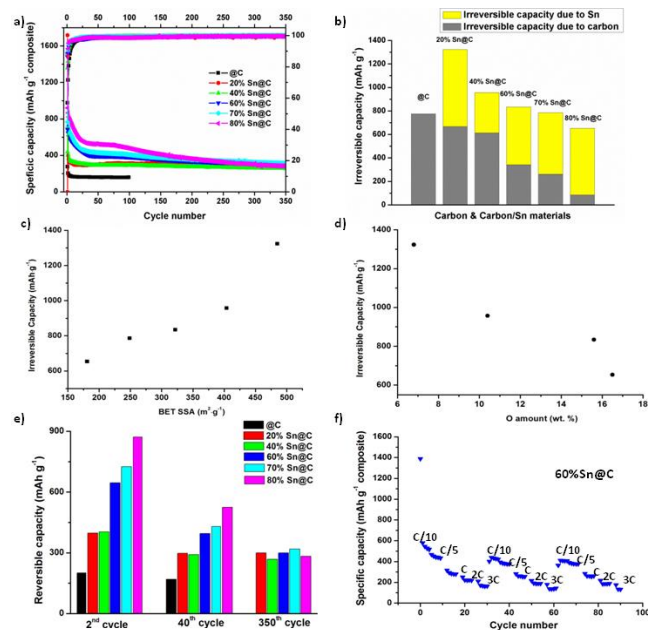


Figure 6. Specific discharge capacity and coulombic efficiency for the carbon and carbon/Sn materials as a function of cycle number at constant current rates C/5 C rate in the voltage range of 0.01–1.5 V (vs. Li/Li*) (a). The irreversible capacity after the first discharge (b). The correlation between the irreversible capacity and BET specific surface area (c) and oxygen amount in Sn/SnO₂ nanoparticles as determined by XPS (d); The reversible capacity after 2 cycles, 40 cycles and 350 cycles, respectively (e). Specific discharge capacity as a function of cycle number at variable current rates between C/10 and 3C (f).

Despite the strong decrease of irreversible capacity by decreasing the carbon fraction and the specific surface area, an important irreversible capacity is still coming from the Sn-contribution. This is often assigned to the electrolyte consumption due to the conversion reaction of SnO₂ into metallic Sn and Li₂O (Eq. 1). If we represent the evolution of the irreversible capacity *versus* the oxygen amount in the Sn/SnO₂ particles (Figure 6d), one can be noticed that the irreversible capacity decreases with the increase of the oxygen amount in the materials, therefore, with the increase of the quantity of SnO₂. At a first glance, this result seems rather unexpected since a higher amount of SnO₂ in the composites is supposed to induce a higher irreversible capacity due to the reaction (1). However, some authors found also that the presence of SnO₂ in Sn/SnO₂ materials is beneficial to limit the SEI formation, to improve the CE and also to provide long term cycling stability [35],[36],[37]. Therefore, the conversion reaction is not the only factor which may affect the irreversible capacity of Sn/SnO₂ materials. The electrolyte decomposition on the surface of small and reactive Sn/SnO₂ nanoparticles, with the formation of SEI layer or the modification of the particle size/morphology during Li⁺ insertion may account as well for the observed irreversible capacity [38],[39],[35].

Concerning the reversible capacity (Figure 6e), this was also significantly improved by increasing the Sn loading from 397 mAh g⁻¹ for 20 wt.% Sn to 871 mAh g⁻¹ for 80 wt.% Sn, respectively. The values are even higher than the theoretical capacities for these materials (Table S1b, Supporting Information) due probably to some synergetic effects between the Sn nanoparticles and the carbon matrix. For high loadings (60, 70 and 80 wt.%) after a drastically decrease of the capacity during the first 20 cycles ($\approx 40\%$), stable capacities of 524, 430,

326 mAh g⁻¹ is maintained up to 80th cycle, respectively. For lower Sn loadings, after the first cycles, the capacity is directly extremely low (~300 mAh g⁻¹), but not so far from the theoretical values (285 and 340 for 20 wt.% Sn and 40% Sn respectively). Another decrease of the capacity occurs after 100 cycles for the higher loadings, which finally present almost the same capacity (≈ 300 mAh g⁻¹) after 350 cycles (Figure 6e). The fading of capacity for the higher loadings could be a consequence of the large amount of agglomerated particles situated outside of the carbon pores, confirmed by STEM (Figure 2). These particles were not properly in contact with the conductive carbon network and non-confined as well in carbon pores to limit their volume expansion/strain during lithiation/delithiation. STEM analysis after cycling were performed for materials with 60 and 80 wt.% of Sn to see how the Sn-based particles were affected during the cycling (Figure 7). Compared to the materials before cycling (Figure 2b, c), the STEM images at this stage indicate that the 60%Sn@C composite better conserves the particles size and dispersion (Figure 7a), while for 80%Sn@C material the agglomerated particles are more present than before cycling (Figure 7b). These post-mortem investigations confirm that a moderate amount of Sn in the porous carbon frameworks is required to balance the particle aggregation, the material conductivity and electrolyte diffusion.

The evolution of the capacity for long cycling could indicate a similar maximal electrochemical potential no matter the Sn NPs loading. Therefore, to choose the most promising material which could be used as anode, we should consider the irreversible capacity, as well as the reversible capacity but not only during the first cycles which presents the highest value for the material with 80 wt.% of Sn, but also the long-term cycling stability behavior, which seems to be influenced, especially, by the dispersion of the particles in the carbon matrix.

The coulombic efficiency of the C/Sn composite materials reaches fast 100% (after 10 cycles), which means that no parasitic reactions take place because of the electrolyte degradation is disappeared after first cycles.

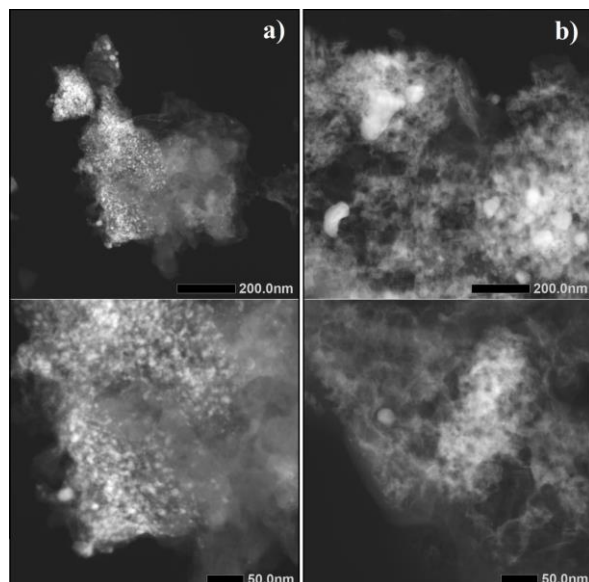


Figure 7. STEM images after 350 cycles for 60%Sn@C (a) and 80%Sn@C (b).

Figure 6f shows the cycling performances of the C/Sn-based materials at different current rates. The reversible discharge capacities of the composites strongly depend on the C rate and thus, for Sn/C composite the values decrease to 578, 466, 314, 249 and 210 mAh g⁻¹ at C/10, C/5, C, 2C and 3C, respectively,

and successfully regain up to 90% from the initial capacity, when the current rate is set back to its initial value.

Conclusions

Mesoporous carbon/Sn-based materials with different Sn loading were prepared by a facile and fast route based on an impregnation/reduction bottom-up approach. For all loadings, a mixture of Sn/SnO₂ was formed and several complementary techniques (Mössbauer spectroscopy, XPS and TGA) were employed to carefully assess their amount and ratio in the carbon matrix to correctly evaluate their impact on the electrochemical performances. At low Sn loadings (< 60%) the Sn NPs are very homogenous dispersed in the carbon network with particle size around 5 nm and only few aggregates observed. The increase of the Sn loading induces the formation of larger Sn particles and many Sn agglomerates (~ 200 nm), which are not embedded in the carbon porosity, as revealed by XRD and TEM. Moreover, the increase of the Sn loading in the carbon framework induces a significant decrease in the textural properties (SSA and pore volume) which could be assigned partly to the Sn density but also to the confinement of Sn particles into the carbon pores. It was evidenced also that the Sn nanoparticles may present a non negligible inter-grain porosity.

The increase of the Sn loading leads to a decrease of the irreversible capacity during the first cycle, which was mainly related to the decrease of the SSA. Improvement of the reversible capacity is achieved as well; however, the evolution of the reversible capacity for long cycling demonstrated significant fading for high loadings triggered by Sn NPs placed outside the carbon pores which undergo severe agglomeration due to volume expansion upon lithiation. Therefore, similar electrochemical performances are reached regardless the Sn NPs loading after 350 cycles. Our findings suggest that a high Sn loading combined to small and dispersed particle size in the carbon framework may be the key factor to achieve high reversible capacity and long term cycling.

Experimental Section

Material synthesis

The mesoporous carbon support was prepared by a soft-template phase separation route as previously reported in our work [21,3], involving the dissolution of phloroglucinol (the carbon source, 1.65g) and Pluronic F-127 (pore generation agent, 3.27 g) in a solution of ethanol (81 mL) containing small quantity of hydrochloric acid (0.6 mL), followed by the glyoxal addition (1.62 mL). The latter one is used as cross-linker to form a tridimensional phenolic resin with phloroglucinol able to self-assemble with the triblockpolymer template Pluronic F-127 via H-bonding giving rise to mesophase nano-assemblies. Thermal annealing at 900°C of organic polymer phase allows to obtain the mesoporous carbon support.

The C/Sn hybrid materials with different Sn loadings (x%Sn@C, where x=20/40/60/70/80) were prepared by liquid impregnation of the porous carbon network (C) with a SnCl₄·5H₂O ethanol solution under stirring for 30 min, followed by a chemical reduction process with NaBH₄ solution in water in order to reduce the SnCl₄·5H₂O to Sn (0.6g NaBH₄/1g SnCl₄·5H₂O). The reducing agent was eliminated by washing the material with distilled water at room temperature. The final material was dried at 80°C for 12h.

Materials characterization

The crystalline structure of the materials was characterized by X-ray powder diffraction (XRD) technique, by using a powder diffractometer D8 ADVANCE A25 from Bruker in Bragg-Brentano reflection geometry $\theta - \theta$. This diffractometer is equipped with the LynxEye XE-T high resolution energy dispersive 1-D detector (Cu $K\alpha_{1,2}$), leading to ultra-fast X-ray diffraction measurements. The X-ray powder diffraction data uses proprietary Bruker format which are converted into usable one via PowDLL 2.71 [26]. The Sn crystallite size was determined using the Scherrer formula and the FWHM (Full Width at Half Maximum) was extracted via DIFFRAC.EVA [27] (Cu $K\alpha_2$ contribution previously removed) and also checked via WinPLOTR profile fitting procedure [40]. The material surface morphology/structure was investigated with a JEOL ARM-200F transmission electron microscope working at 200 kV. EDX mapping was obtained with a JED 2300 detector. Thermogravimetric analyses (TGA) were conducted on a TGA 851 (Mettler-Toledo) thermogravimeter by heating the samples under air (100 ml/min), from 30°C up to 900°C with a 10 °C/min heating rate.

^{119}Sn Mössbauer spectra were collected with a constant acceleration spectrometer using a $\text{Ca}^{119\text{m}}\text{SnO}_3$ source in the transmission geometry. They were fit by combinations of Lorentzian lines. The absorber used for the determination of the hyperfine parameters contained 120 mg cm^{-2} of the Sn composite. The velocity scale is calibrated with a ^{57}Co source and a pure iron foil absorber. The isomer shifts are given relative to BaSnO_3 standard at room temperature. The absorption areas were further used to calculate the quantities of Sn and SnO_2 loaded in the carbon/Sn hybrid materials. Lamb-Mössbauer factors of 0.5 and 0.05 have been assumed for the conversion of absorption areas for SnO_2 and Sn, respectively [32]. X-ray photoelectron spectroscopy (XPS) was performed with a VG Scienta SES 200-2 spectrometer equipped with a monochromatized Al $K\alpha$ X-ray source (1486.6 eV) and a hemispherical analyzer. The pass energy was 100 eV.

The textural properties of the carbon and carbon/Sn hybrid materials were evaluated using N_2 adsorption/ desorption isotherms measured with a Micromeritics ASAP 2420 device at 77K. The samples were out-gassed in vacuum at 80°C for 12 h before the adsorption analysis. The specific surface area (SSA) was calculated from the linear plot in the relative pressure range of 0.01-0.05. The micropore volume (V_{micro} , pore size < 2 nm) was obtained using the Dubinin-Radushkevich (DR) equation in the relative pressure interval (P/P_0) from 10^{-4} to 10^{-2} . The total pore volume (V_T) was determined from the amount of nitrogen adsorbed at a relative pressure of 0.95. The mesoporous volume (V_{meso} , 2nm < pore size <50 nm) was determined by subtracting the microporous volume from the total pore volume. The pore size distributions (PSD) were determined from the adsorption branch of nitrogen isotherms using the 2D NLDFT heterogeneous surface model for carbon materials implemented in SAIEUS (Micromeritics) [41].

Electrochemical characterization

The electrode preparation was made by mixing in a jar the synthesized materials (70%) with carbon black (10%) and vapor grown carbon fibers - VGCF-S (10%) as conductive additive, and carboxymethylcellulose - CMC (10%) as binder. A quantity of 0.4 ml distilled water was added over the materials and homogeneously mixed by ball-milling for 1h. The film with a thickness of 100 μm was laid down on a copper foil, dried at room temperature for 4h and at 100°C under vacuum for other 12h. The electrochemical results were calculated based on the active mass, which was considered the mass of the carbon/Sn/ SnO_2 composite. The corresponding loading of the active mass in the electrode was comprised between 0.9 and 1.9 mg/cm^2 .

The electrochemical performances of carbon and carbon/Sn-based materials as negative electrode for Li-ion batteries were

studied in coin cells assembled in an argon filled glove box. The electrolyte used for the coin cell preparation was LiPF_6 with ethylene carbonate (EC), propylene carbonate (PC), dimethyl carbonate (DMC) (1:1:3) as solvents and vinyl carbonate (VC)(1%) and fluoro ethylene carbonate (FEC)(5%) as additives. The galvanostatic charge and discharge measurements were carried out at room temperature on Neware battery testing system (BTS3000) at room temperature. The capacity is reported per gram of C/Sn composite.

Acknowledgements

The authors gratefully acknowledge the financial support of this work from University of Haute-Alsace, France through the Ph.D. scholarship of Cristina Nita. We thank Loic Vidal and Samar Hajjar for STEM and XPS analyses performed via the IS2M Mulhouse technical platform.

Keywords: carbon/Sn hybrids; mesoporous carbon; tin-based nanoparticles; Li-ion batteries.

References

- [1] J.-M. Tarascon, M. Armand, *Nature* **2001**, 414, 359-367.
- [2] H. Tavassol, M. W. Cason, R. Nuzzo, A. Gewirth, *Adv Mater Lett* **2011**, 5, 1400317.
- [3] A. Jahel, C. Matei Ghimbeu, L. Monconduit, L. Vix-Guterl, *Adv.Energ.Mater.* **2014**, 4, 1400025.
- [4] F. Courtel, Abu-Lebdeh, in *Nanotechnology for Lithium-Ion Batteries*, Springer, Boston, MA **2012**, 67-83.
- [5] B. Wang, B. Luo, X. Li, L. Zhi, *Mater Today* **2012**, 15, 544-552.
- [6] C. Kim, M. Noh, M. Choi, J. Cho, B. Park, *Chem Mater* **2005**, 17, 3297-3301.
- [7] G. Du, C. Zhong, P. Zhang, Z. Guo, Z. Chen, H. Liu, *Electrochem Acta* **2010**, 55, 2582-2586.
- [8] Y. Zhong, X. Li, R. Zhang, R. Li, M. Cai, X. Sun, *Appl Surface Science* **2015**, 332, 192-197.
- [9] X. Bai, B. Wang, H. Wang, J. Jiang, *J Alloys Compd* **2015**, 628, 412.
- [10] G. Guo, Q. Yang, J. Liang, L. Wang, Y. Zhu, Y. Qian, *Mater Lett* **2016**, 184, 332-335.
- [11] S. Liang, X. Zhu, P. Lian, W. Yang, H. Wang, *J Solid State Chem* **2011**, 184, 1400-1404.
- [12] B. Veeraraghavan, A. Durairajan, B. Haran, B. Popov, R. Guidotti, *J Electrochem Soc* **2002**, 2002, 675-681.
- [13] Y. Xu, Y. Zhu, Y. Liu, C. Wang, *Adv Energy Mater* **2013**, 3, 128-133.
- [14] C. Liu, H. Huang, G. Cao, F. Xue, R. Paredes Camacho, X. dong, *Electrochimica Acta* **2014**, 144, 376-382.
- [15] M. Wu, C. Wang, J. Chen, F. Wang, B. Yi, *Ionics* **2013**, 19, 1341-1347.
- [16] S. Han, J. Xu, B. Li, G. Liu, G. Song, Z. Guo, *Matter Lett* **2017**, 199, 93-96.
- [17] C. Cui, X. Liu, N. Wu, Y. Sun, *Mater Lett* **2015**, 143, 35-37.
- [18] P. Wu, N. Du, H. Zhang, J. Yu, Y. Qi, D. Yang, *Nanoscale* **2011**, 3, 746-750.
- [19] I. Meschini, F. Nobili, M. Manchini, R. Marassi, R. Tossici, A. Savoini, M. Focarete, F. Croce, *J Power Sources* **2013**, 226, 241-248.
- [20] X. Liu, X. Li, J. Yu, Y. Sun, *Matter Lett* **2018**, 223, 203-206.
- [21] A. Jahel, C. Matei Ghimbeu, A. Darwiche, L. Vidal, S. Hajjar-Garreau, C. Vix-Guterl, L. Monconduit, *J Mater Chem A* **2015**, 3, 11960-11969.
- [22] Y. Wang, Z. Ma, C. Lu, *Composite Interfaces* **2016**, 23, 273-280.
- [23] J. Ren, J. Yang, A. Abouimrane, D. Wang, K. Amine, *J Power Sources* **2011**, 196, 8701-8705.
- [24] X. Chang, T. Wang, Z. Liu, X. Zheng, J. Zheng, X. Li, *Nano Res* **2017**, 10, 1950-1958.

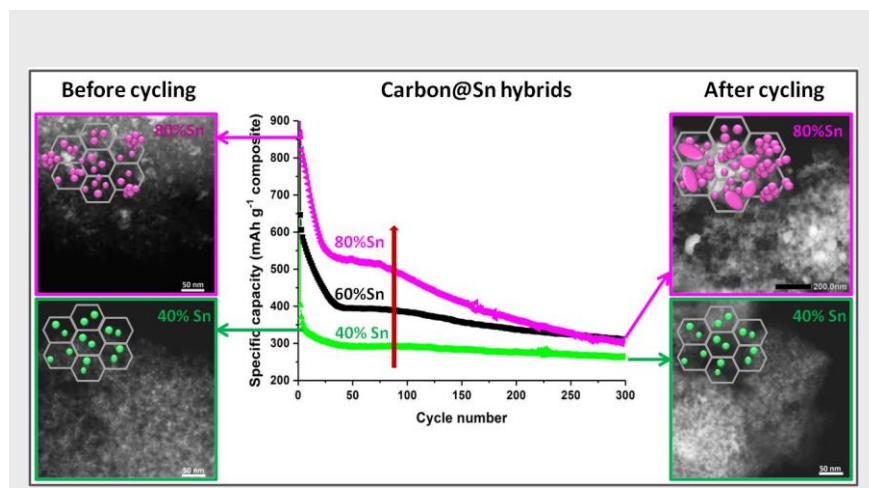
-
- [25] C. Matei Ghimbeu, C. Zlotea, R. Gadiou, F. Cuevas, E. Leroy, M. Latroche, C. Vix-Guterl, *J.Mater.Chem.* **2011**, 21, 17765-17775.
- [26] N. Kourhoulmelis, *ICDD Annu.Spring Meet.Ed Lisa O'Neill Powder Diffr.* **2013**, 28, 137-148.
- [27] P. Caussin, J. Nusinovici, D. W. Beard, *Adv.X-ray Anal.* **1988**, 31, 423-430.
- [28] P. Scherrer, *Gött.Nachr.* **1918**, 2, 98-100.
- [29] C. Zlotea, Y. Oumellal, S.-J. Hwang, C. Matei-Ghimbeu, P. Jongh, M. Latroche, *J Phys Chem C* **2015**, 119, 18091-18098.
- [30] S. Sun, C. Matei Ghimbeu, Vix-Guterl-C, M.-T. Sougrati, C. Masquelier, R. Janot, *J Power Sources* **2015**, 284, 574-581.
- [31] E. Sutter, F. Ivars-Barcelo, P. Sutter, *Part.Part.Syst.Character.* **2014**, 31, 879-885.
- [32] M. Sourgati, S. Jouen, B. Hannyoyer, *Hyperfine Interact* **2006**, 167, 815-818.
- [33] S. Böhme, B. Philippe, K. Edström, L. Nyholm, *J Phys Chem C* **2017**, 121, 4924-4936.
- [34] G. Wang, B. Wang, X. Wang, J. Park, S. Dou, H. Ahnb, K. Kimb, *J Mater Chem* **2009**, 19, 8378-8384.
- [35] M. Inaba, T. Uno, A. Tasala, *J Power Sources* **2005**, 146, 473-477.
- [36] K. Chiu, H. Lin, K. Lin, *J Electrochem Soc* **2006**, 2006, A1038-A1042.
- [37] A. Sivashanmugam, T. Kumar, N. Renganathan, S. Gopukumar, Wohlfahrt-Mehrens, J. Garche, *J Power Sources* **2005**, 144, 197-203.
- [38] R. Hu, H. Liu, M. Zeng, J. Liu, *Chin Sci Bull* **2012**, 57, 4119-4130.
- [39] S. Beattie, T. Hatchard, A. Bonakdarpour, K. Hewitt, J. Dhan, *J Electrochem Soc* **2003**, 150, A701-A705.
- [40] T. Roisnel, J. Rodriguez-Carvajal, *Materials Science Forum, Proceedings of the Seventh European Powder Diffraction Conference (EPDIC 7)* **2000**, Ed. R. Delhez and E.J. Mittenmeijer, 2000, 118-123.
- [41] J. Jagiello, J. Olivier, *Carbon* **2013**, 55, 70-80.
-

Table of Contents

Understanding the Sn loading impact on the performances of mesoporous carbon/Sn based nanocomposites in Li-ion batteries

Cristina Nita ^{[a],[b]}, Julien Fullenwarth ^{[c],[d]}, Laure Monconduit ^{[c],[d]}, Jean-Marc Le Meins ^[a], Julien Parmentier ^[a], Moulay Sougrati ^{[c],[d]}, Camélia Matei Ghimbeu ^{[a],[d]}*

Page No. – Page No.



Sn loading affects the size and dispersion of Sn nanoparticles and is the key parameter to ensure long term battery cycling performances.
